

CHAPTER IV

EXPLORING THE SPACE-TIME STRUCTURE OF THE FIREBALL

As already emphasized in Ch. II, understanding the dynamical space-time picture of the heavy-ion collisions is important for interpreting the final stage observables from experimental data for EoS and the critical behavior studies.

We will begin this chapter by demonstrating the influence on the cluster formations, particularly the simplest cluster deuteron and antideuteron, from the freeze-out geometry of the fireball. We explore the fireball geometry across beam energy spectra to investigate the possible critical behavior on the source volume. Then UrQMD transport model will be employed to validate our findings.

Later on, we further our fireball volume investigation by studying the fireball space-time geometries from the effects of various phase transition scenarios, i.e., from different EoS using the HBT radii. The HBT radii are equivalent to the interpretation of the emission source for these clusters and they are related to the expansion time.

Overall, in this Ch. IV we present comprehensive studies on the space-time structure of the fireball from various beam energies and various EoS using the cluster formations and HBT radii.

Clusters are final stage observables and one of the most direct probes for such studies. Clusters are composed particles of nucleons. Their formations are sensitive to critical phenomena due to the fact that their constituents, nucleons, are subjected to baryon conservation. At the critical point, it is well known that all conserved quantities will diverge at chemical freeze-out. This leads to the divergence of the correlation length, fluctuation, and susceptibilities of the conserved quantities. The divergence of correlation length and fluctuation of the nucleons will influence the formation of the clusters at the kinetic freeze-out. These divergences are also related to the compression and expansion of the source volume, fireball.

However, these physical interpretations could only be manifested and investigated with the proper choice of formation mechanisms. The coalescence model states that if two or more nucleons are close enough in phase-space, they will coalesce and form a cluster at the very last stage of collisions, kinetic freeze-out (for more

details, see Ch. V). This physical description, on the space-time localization of the coalescence model, makes it suitable for our following studies. It allows us to investigate their emission sources and constituent density profiles and the all influences before their emission at kinetic freeze-out.

Back in 1992, the deviations from the simple approach were reported with the failure to predict antideuteron yield in Si+Au collisions at AGS (Aoki et al., 1992), where the measured antideuteron invariant cross section is suppressed by 5-10 times compared to the deuteron's. Since the simple coalescence dictates the cluster formation mainly by a single coalescence parameter B_2 , the formation of deuterons and antideuterons are expected to yield similar amount. This inconsistency leads to the development of the phase-space coalescence approach.

The failure to describe the suppression of antideuterons was attributed to the dependency of deuteron (Sato and Yazaki, 1981; Remler, 1981; Mrowczynski, 1987; Lyuboshits, 1988; Danielewicz and Schuck, 1992; Mrowczynski, 1992) and antideuteron (Mrowczynski, 1990; Dover et al., 1991; Leupold and Heinz, 1994) formation rates to the emission-source geometries in nuclear collisions. Then S. Mrówczyński proposed the geometrical space-time formation rate to address the phase-space coalescence model (Mrowczynski, 1993).

His approach assumed that antinucleons are emitted from the outer shell of the source due to a high probability of nucleon-antinucleon annihilation in the central baryon-rich region, while nucleons are emitted from the entire volume. Despite assuming spherical symmetry, this model successfully described experimental data from Si+Au collisions at $E_{\text{lab}} = 14.6A$ GeV (Aoki et al., 1992).

In the next section, we will apply the antideuteron and deuteron formation by Mrówczyński coalescence approach to reconstruct and explore the size of the emission source, assuming spherically symmetric (anti)nucleon source functions and call this approach “Mrówczyński coalescence model”.

4.1 (Anti)deuteron formation rate and source geometry

The original Mrówczyński coalescence model (Mrowczynski, 1993) purposed that the shape of the antinucleons source has to be reconsidered as well as suggesting an analytic formula to get rid of the un-measurable constant parameter p_0 . The (anti)deuteron distributions and (anti)nucleon distributions can then be formulated according to the tunable space-time parameter which can be related to the collision

system's initial conditions.

4.1.1 Mrówczyński Density Function

The main assumption of this approach is that the produced antinucleons located close to the center of the collision have a substantial probability to experience secondary interactions and annihilation in the baryonic rich environment. Antinucleons produced on the closer to the surface, on the other hand, have a higher chance to escape the fireball and proceed to coalescence. Nucleons are emitted from the whole source or fireball volume. From the above picture, we can impose and modify different geometries on the antinucleon and nucleon sources which can help us addressing the difference formation rates.

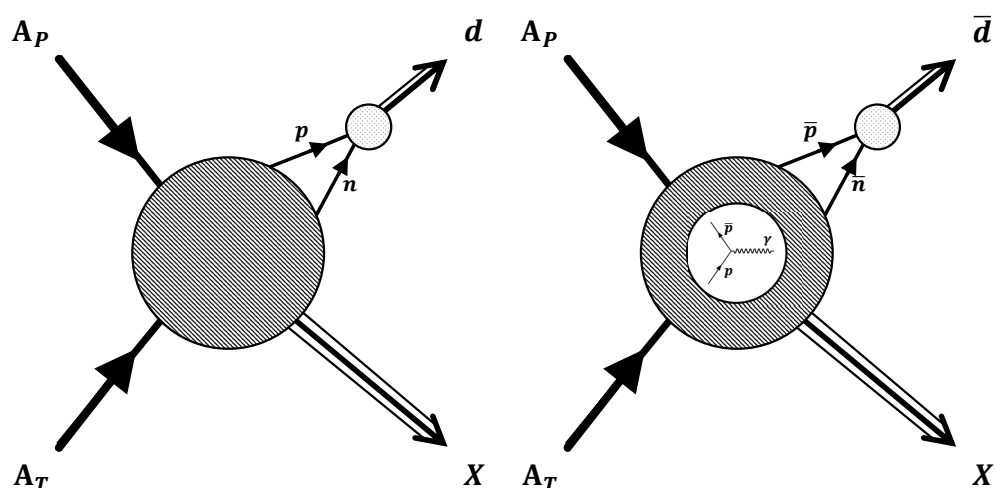


Figure 4.1 The schematic picture of the geometric coalescence model for (anti)deuteron formation if the two (anti)nucleons are close enough in phase-space. A_p and A_T are the incoming projectile and target nucleons and X represents the particles that carry the rest momenta of the system. (Left) The nucleon emission source is a whole spherical with radius r_0 . (Right) the survived antinucleons are emitted only on a spherical shell radius r_0 as the $N\bar{N}$ annihilations destroy most of the antinucleon at the center radius r_* .

The simple coalescence model describes the formation of clusters assuming that a pair of final-state (anti-)nucleons carrying similar momenta can coalesce to form a deuteron or an antideuteron with total momentum P . The invariant differential production cross sections for deuterons (d) and nucleons (p) and accordingly for

antideuterons and antinucleons are related by

$$E \frac{d^3\sigma_d}{dP^3} = B_2 \left(\frac{E}{2} \frac{d^3\sigma_p}{d(P/2)^3} \right)^2, \quad (4.1)$$

where (E, \vec{P}) and $(E/2, \vec{P}/2)$ denote the deuteron and nucleon 4-momenta and σ_{inel} is the total inelastic cross section. The coalescence parameter B_2 can be measured in experiments and is usually used to infer the volume of the source size. Then, Mrówczyński coalescence states that the formation rate is related to this coalescence parameter via $\mathcal{A} = \frac{m}{2} B_2$, with m denoting the nucleon mass. The formation rate \mathcal{A} is calculated as

$$\mathcal{A} = \frac{3}{4} (2\pi)^3 \int \int d^3r_1 d^3r_2 \mathcal{D}(\vec{r}_1) \mathcal{D}(\vec{r}_2) |\Psi_d(\vec{r}_1, \vec{r}_2)|^2, \quad (4.2)$$

where the bulk nucleon source $\mathcal{D}(\vec{r}_i)$ describes the probability of finding one nucleon at a given point \vec{r}_i in kinetic freeze-out fireball (volume emission) and $\Psi_d(\vec{r}_1, \vec{r}_2)$ denotes the deuteron wavefunction. The emitted nucleons are assumed to be uncorrelated.

Figure 4.1 shows the emission regions for (anti)nucleons, the nucleon source is distributed over the whole fireball, while the antinucleons are suppressed near the center of the whole volume. This leads to a surface-like to shell-like emission source for antinucleon's. The nucleon source function $\mathcal{D}(\vec{r})$ is parametrized by a normalized Gaussian (Mrowczynski, 1993),

$$\mathcal{D}(\vec{r}_i) = \frac{\exp(-\vec{r}_i^2/2r_0^2)}{(2\pi)^{3/2} r_0^3}, \quad (4.3)$$

with r_0 given by the mean radius squared $\langle r^2 \rangle = 3r_0^2$. The normalized antinucleon source function $\overline{\mathcal{D}}(\vec{r})$ contains a second Gaussian of width r_* that effectively cuts out the central region reads as

$$\overline{\mathcal{D}}(\vec{r}_i) = \frac{\exp(-\vec{r}_i^2/2r_0^2) - \exp(-\vec{r}_i^2/2r_*^2)}{(2\pi)^{3/2} (r_0^3 - r_*^3)}. \quad (4.4)$$

It is useful to simplify our analysis into the center of mass frame coordinates, $\vec{P} = \vec{p}_1 + \vec{p}_2$, $\vec{R} = \frac{1}{2} (\vec{r}_1 + \vec{r}_2)$ with relative motions, $\vec{p} = \frac{1}{2} (\vec{p}_1 - \vec{p}_2)$, $\vec{r} = \vec{r}_1 - \vec{r}_2$.

The deuteron wavefunction then factorizes to

$$\Psi_d(\vec{r}_1, \vec{r}_2) = \exp(i\vec{P}\cdot\vec{R})\phi_d(\vec{r}), \quad (4.5)$$

The Hulthén wavefunction reads

$$\phi_d(\vec{r}) = \left(\frac{\alpha\beta(\alpha + \beta)}{2\pi(\alpha - \beta)^2} \right)^{1/2} \frac{\exp(-\alpha r) - \exp(-\beta r)}{r}, \quad (4.6)$$

with parameters $\alpha = 0.23 \text{ fm}^{-1}$ and $\beta = 1.61 \text{ fm}^{-1}$ (Hodgson et al., 1997). The formation rate \mathcal{A} in relative coordinates then reads,

$$\mathcal{A} \equiv \frac{3}{4}(2\pi)^3 \int d^3r \mathcal{D}_r(\vec{r}) |\phi_d(\vec{r})|^2, \quad (4.7)$$

where the nucleon source function is

$$\mathcal{D}_r(\vec{r}) = \frac{1}{(4\pi)^{3/2} r_0^{3/2}} \exp(-r^2/4r_0^2), \quad (4.8)$$

and the antinucleon source function is

$$\overline{\mathcal{D}}_r(\vec{r}) = \frac{r_0^3 e^{-\frac{r^2}{4r_0^2}} + r_*^3 e^{-\frac{r^2}{4r_*^2}} - \frac{2^{\frac{5}{2}} r_0^3 r_*^3}{(r_0^2 + r_*^2)^{3/2}} e^{-\frac{r^2}{2(r_0^2 + r_*^2)}}}{(4\pi)^{3/2} (r_0^3 + r_*^3)^2}. \quad (4.9)$$

The antideuteron formation rate $\overline{\mathcal{A}}$ as function of r_0 is depicted in Figure 4.2. When the suppression region $r_* = 0 \text{ fm}$, the antideuteron formation rate is identical to the deuteron formation rate. As the size of the suppression region r_* increases at the same source size r_0 , the antideuteron formation rate decreases. This decrease is attributed to the thinning of the antideuteron emission shell as the suppression region expands.

4.2 Energy Dependence of Formation Geometry

To extract the energy-dependent geometries of the antideuteron and deuteron sources, we first determine the deuteron emission source radius r_0 by fitting the coalescence parameter B_2 from various experiments, as it is proportional to

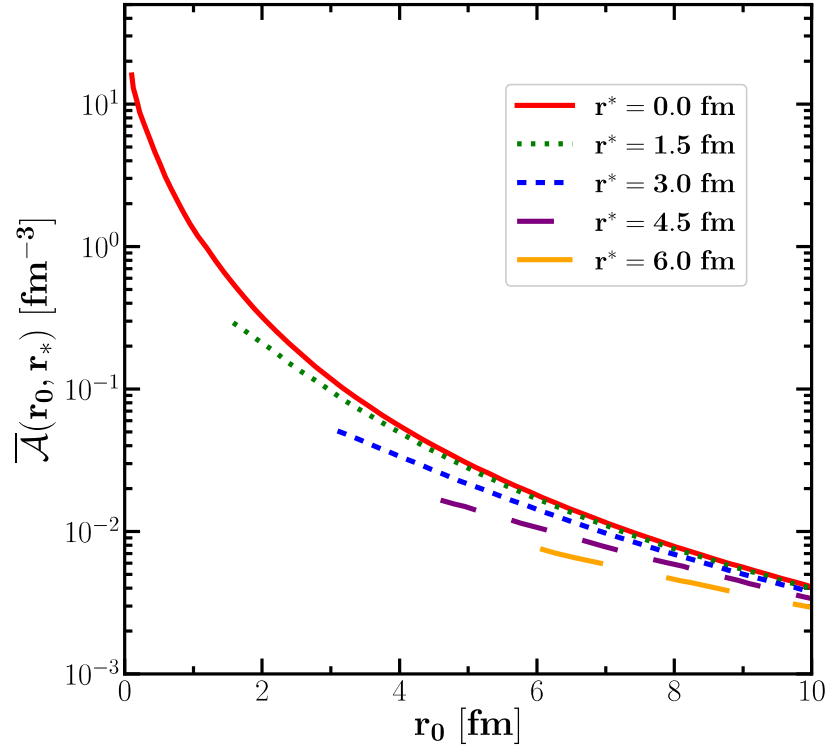


Figure 4.2 The antideuteron formation according to the source bulk radius r_0 with varying suppression radii r_* .

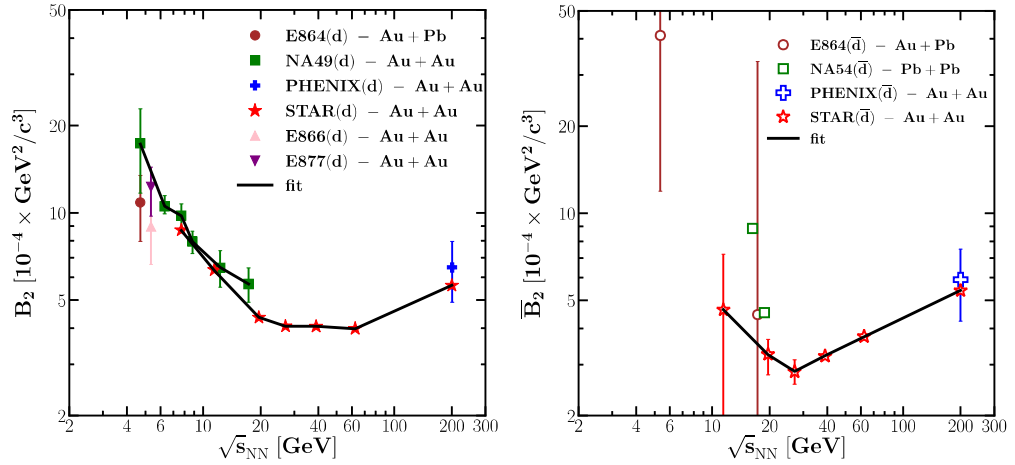


Figure 4.3 The energy dependence coalescence parameters B_2 for deuterons (left) and \bar{B}_2 antideuterons (right) from various experiments ranging from $\sqrt{s_{NN}} = 4.7 - 200$ GeV. The black lines show the B_2 and \bar{B}_2 fits using the extracted radii r_0 and r_* according to the formation rate in Eq. (4.7)

the deuteron formation rate $\mathcal{A}(\vec{r}, r_0)$. The fit results for experiments such as NA49 and STAR are illustrated in Figure 4.3 (left) as black lines. Next, we extract the suppression region of the antideuteron source r_* by fitting the antideuteron coalescence parameters $\overline{B}_2 \propto \overline{\mathcal{A}}(\vec{r}, r_0, r_*)$ to the experiments shown in Figure 4.3 (left). We assume that both deuteron and antideuteron share the same emission source radius r_0 . This process allows us to characterize both the emission source r_0 and the suppression region r_* , providing insights into the energy dependence of formation geometries.

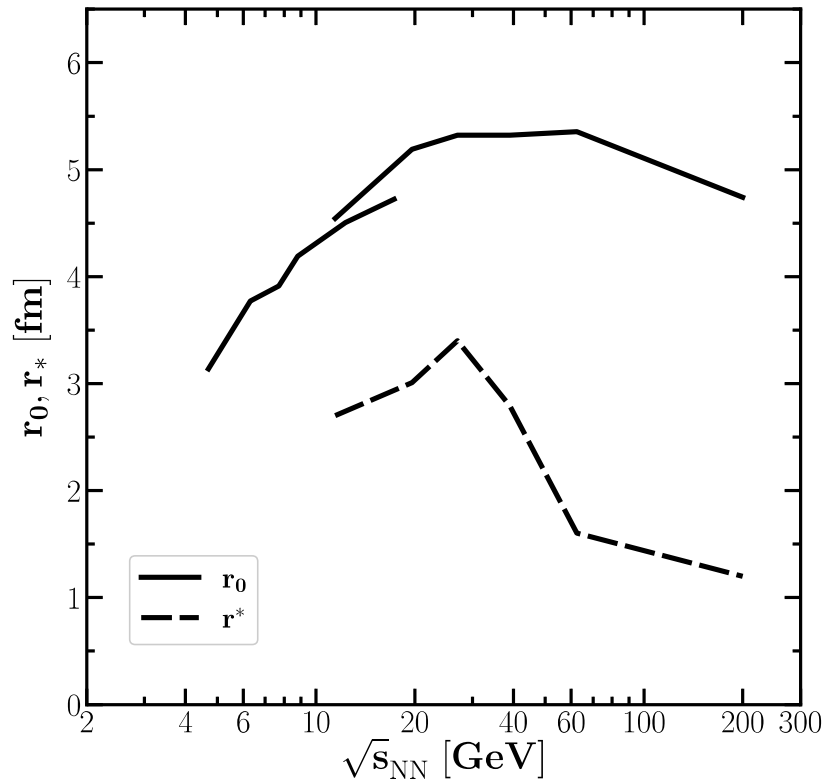


Figure 4.4 The emission source radius r_0 of deuteron (solid black lines) and the suppression region of antideuteron source r_* (dash-dotted line) as a function of energy

The energy dependence of the extracted source radii is presented in Figure 4.4. The deuteron emission source and also the antideuteron outer radius r_0 (solid black lines) exhibit rapid growth with increasing center-of-mass energy below $\sqrt{s_{NN}} = 20$ GeV. The extracted radii r_0 from NA49 and STAR experiments show good agreement with a smooth connection with respect to the center-of-mass energy. However, the growth is suppressed and declines after reaching a maximum at $\sqrt{s_{NN}} = 63$ GeV. The flattening and subsequent decrease in B_2 and r_0 for energies $\sqrt{s_{NN}} \geq 20$ GeV contradict the assumption that a volume of the emission source, i.e.,

a fireball, increases with energy. This phenomenon may be attributed to flow effects, as reported in Ref. (Gaebel et al., 2021).

Regarding the annihilation region, i.e., the inner radius r_* (depicted as a dash-dotted line), it similarly exhibits an increase at low energies followed by a drop after reaching a maximum at $\sqrt{s_{\text{NN}}} = 27$ GeV. This trend might suggest a nutcracker-like shell structure in this energy regime, as speculated by Ref. (Shuryak, 1999). The decrease in the inner radius implies that antideuterons have a higher probability of survival inside the fireball. This can be explained by the dominance of pions over nucleons in the fireball at this energy regime, significantly reducing the annihilation cross section of $N\bar{N}$.

4.3 Validation with UrQMD

For theoretical validation of the source geometries, we conducted simulations using the Ultrarelativistic Quantum Molecular Dynamics (UrQMD) transport model. Serving as a realistic microscopic simulation, UrQMD tracks the propagation of each hadron's 4-coordinates and 4-momenta from the initial collisions until the last collisions at kinetic freeze-out, accounting for all re-scatterings, annihilations, and decays. To confirm our interpretations of the nucleon and antinucleon source geometries and extract the corresponding parameters, we simulate 0 — 10% central Au+Au collisions at various collision energies ranging from $\sqrt{s_{\text{NN}}} = 7.7$ to 200 GeV. The nucleon and antinucleon distributions are examined in the transverse plane r_T given by $\frac{1}{r_T} \frac{dN}{dr_T}$, where $r_T = \sqrt{r_x^2 + r_y^2}$, the normalization by $1/r_T$ accounting for a cylindrical geometry at mid-rapidity. The expression of the (anti)nucleon distribution is

We present examples of the normalized transverse distribution r_T of (anti)nucleons at $\sqrt{s_{\text{NN}}} = 11.5$ and 200 GeV in Figure 4.5. In the case of $\sqrt{s_{\text{NN}}} = 11.5$ (left panel), within the range $r_T \leq 5$ fm, nucleons experience a slight suppression around 5% below the maximum. Conversely, the suppression of antinucleons is notably stronger, amounting to around 80%.

At the higher energy of $\sqrt{s_{\text{NN}}} = 200$ GeV (the right panel), both nucleons and antinucleons exhibit comparable suppression levels, approximately 60 — 70% at the core of the sources. This indicates that, across different energy regimes, both antinucleons and nucleons experience some kind of suppression at the core. For the nucleons, this is due to the increased production of other particles at the core of the fireball, particularly pions, which become dominant at higher energies. However, the degree of antinucleon suppression reflects nucleon-antinucleon annihilation. At high

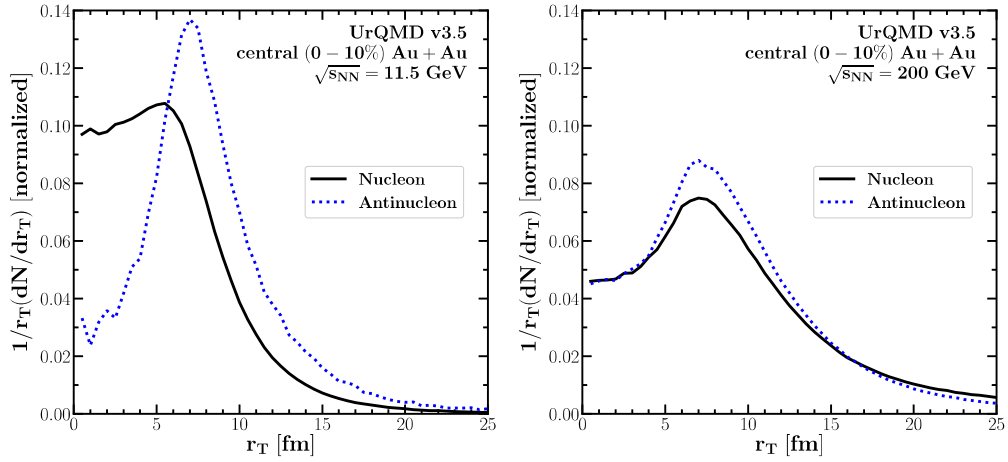


Figure 4.5 The normalised (anti)nucleon distribution in transverse plane r_T at $\sqrt{s_{NN}} = 11.5$ GeV (left panel) and $\sqrt{s_{NN}} = 200$ GeV (right panel). The black solid line represents the nucleon distribution and antinucleon distribution is depicted with the dotted line.

energies, the annihilation probability is reduced because the nucleon distribution is scarcer compared to lower energies reducing the suppression of antinucleons at the core.

After analyzing the quantitative distributions of both nucleon and antinucleon sources, we can extract the source geometries by fitting the nucleon and antinucleon distributions with Gaussian source functions $\mathcal{D}(r_0)$ and $\overline{\mathcal{D}}(r_0, r_*)$, respectively. We assume a simple non-suppressed source function for the nucleons. Additionally, the outer source radii of nucleons and antinucleons are assumed to be independent and fitted separately.

The extracted freeze-out geometries of (anti)nucleons shown in Figure 4.6 support the idea that nucleon-antinucleon annihilation is suppressed due to the pion enhancement at high energy, as evidenced by the drop in the inner radius r_* (open blue squares) with increasing energy. Furthermore, we observe that all the extracted radii exhibit a monotonic behavior with energy. This is in contrast to the sources extracted from the Mrówczyński coalescence model fitted with experimental data, which exhibit local maxima for both the shared r_0 and r_* of the antinucleon source. This might be attributed to using the cascade mode in UrQMD which lacks critical behavior as the EoS is turned off. The sizes of the nucleon source radius r_0 (full black circles) are comparable to the sizes of the antinucleon source's outer radius r_0 (full blue squares). This supports

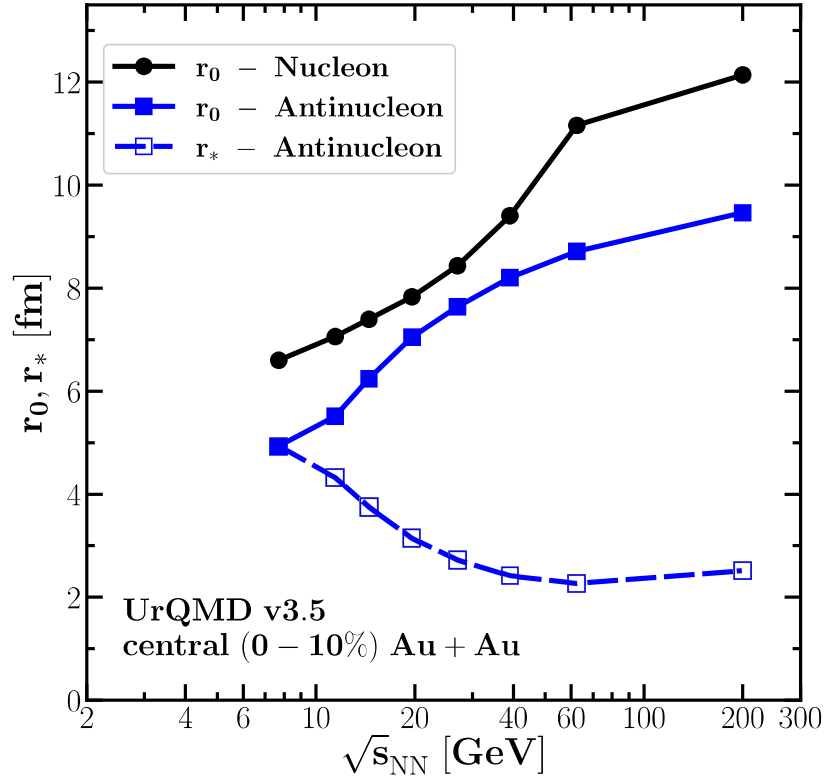


Figure 4.6 The energy dependence of the fitted (anti)nucleon source radii is illustrated. The solid circles represent the whole nucleon source radius r_0 . The extracted source radii of antinucleons are depicted with square symbols. The outer source radius of antinucleons r_0 is represented by the full symbols, while the inner source radius of the suppression region r_* is indicated by the open symbols.

our previous assumption that the antinucleon source shares the same source as nucleons, or at least, is very close around $r_0 \simeq 5 - 12$ fm. Although this value is twice that of the Mrówczyński nucleon source, it is understandable as in UrQMD, the (anti)nucleons gradually freeze out, while the Mrówczyński model assumes instantaneous emission.

In light of these differences, the qualitative comparison of the antinucleon source from two different approaches is undertaken by examining the r_*/r_0 ratio in Figure 4.7. It is expected that the r_*/r_0 ratio will approach or reach unity at the lowest energy, indicating complete suppression of antinucleon emission. While the results from the Mrówczyński coalescence model (red star symbol) cannot fully support this notion due to the lack of available experimental data at low energy $\sqrt{s_{NN}} < 10$ GeV, the ratio from UrQMD simulations (blue square symbol) does indeed converge to unity at $\sqrt{s_{NN}} = 7.7$ GeV. Furthermore, the overall trends from both approaches align well, as

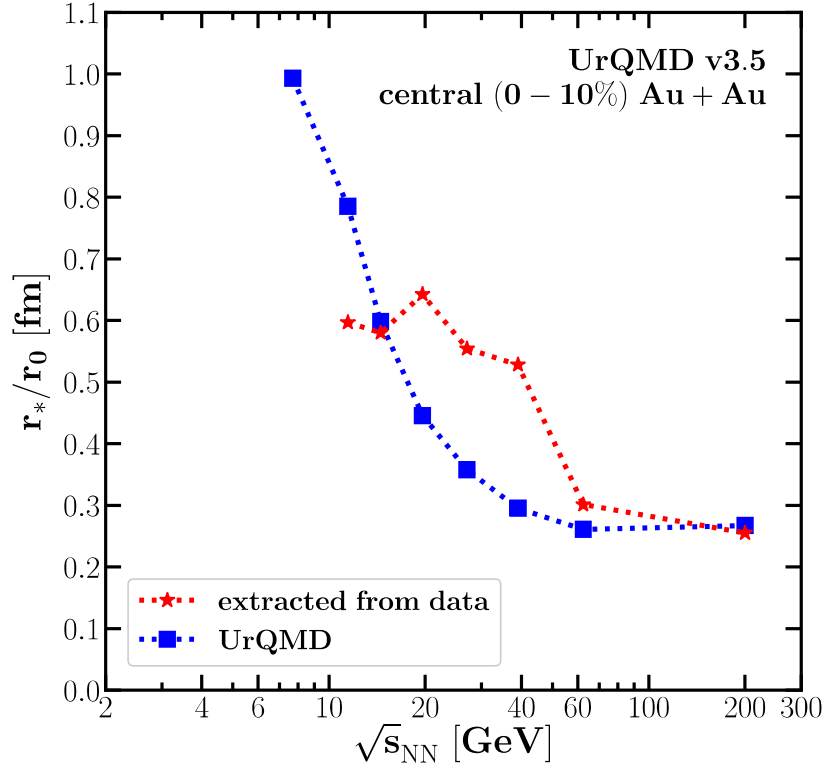


Figure 4.7 The energy dependence of the r_*/r_0 ratio of antinucleon source from Mrówczyński coalescence model (red star symbol) and UrQMD simulation (blue square symbol) at central 0 — 10% Au+Au collisions.

the ratios decrease with increasing energy, supporting the idea of reduced suppression from nucleon-antinucleon annihilation due to the dominance of pion enhancement in the fireball at high energy.

In conclusion, we have presented the Mrówczyński coalescence model which assumes an annihilation region inside the antinucleon source and extracted the (anti)nucleon source radii of r_0 and r_* by fitting the (anti)deuteron formation rate with available experimental data of B_2 and \overline{B}_2 from NA49 to STAR. Comparison with UrQMD supports the idea of suppression inside the core especially for the antinucleons at low energy. For high energy, the nucleon-antinucleon annihilation is suppressed due to the pions dominating the fireball as seen by the transverse distribution and the drop of r_* . Finally, the comparison of r_*/r_0 shows that both models share the same trend as UrQMD's ratio starts at unity at low energy as expected and both ratios decrease with energy. The disappearance of the local maximum of the ratio in UrQMD is attributed by the fact that we employ the cascade mode in UrQMD, so there is no critical behavior

from the change of the EoS. It would be interesting to test our model and the effects of the EoS within UrQMD in the future when experimental data at lower energies becomes available.

So far, we have demonstrated the interplay between the cluster formations and source volume which is crucial for understanding the QCD matter revolving around the critical point and first-order phase transition. The result has hinted at the possibility of critical behavior in the fireball volume measured by the coalescence parameter $B_2(\overline{B_2})$, contrasting with results from the (cascade) UrQMD model.

To deepen our understanding on the effects on the source volume from a phase transition, particularly at low energies, we turn to HBT interferometry (Lacey, 2015; Bluhm et al., 2020), specifically focusing on pion intensity (Pratt, 1986). HBT offers various unique observables sensitive to the first order phase transition, allowing us to probe the critical behavior of the (emission) source volume via the space-time structure and momentum correlations (Ackermann et al., 2003; Csorgo et al., 2006).

The investigations into the effects of the EoS on HBT interferometry within different models are mostly limited to high energies (Pratt, 1986; Bertsch et al., 1988; Ma et al., 2006). Moreover, at high beam energies, other observables like fluctuations haven't exhibited the anticipated behavior indicative of a phase transition. These intensify the debate surrounding the existence of the critical point.

The following section aims to study the interplay between phase transitions and HBT source volumes, with different phase transition scenarios or EOS toward lower energies.

4.4 HBT Correlation

The principle of HBT interferometry proposed by R. Hanbury-Brown and R. Q. Twiss in 1954 (Brown and Twiss, 1956) has become a useful tool in the study of the space-time geometry of the emission sources in astronomy (Hanbury Brown and Twiss, 1956), and nuclear and particle physics (Goldhaber et al., 1960; Csorgo, 2006).

The main difference between the HBT interference and the conventional Michelson interferometry is that the latter one is based on the superposition of two amplitudes. The interference pattern is predicted simply by the path difference between two sources as a function of relative angle. In contrast, the HBT interference occurs by correlating two wave intensities which can also result in intensity distributions as a function of the relative angle between the detectors. Thus, HBT interferometry

can also be understood as intensity interferometry (Wiedemann and Heinz, 1999).

4.4.1 Two-Particle Correlations

The effect of HBT correlations is strongly related to the flow (Dinh et al., 2000; Retiere and Lisa, 2004; Lisa et al., 2005) which can be used to hint at a phase transition (Spieles and Bleicher, 2020). Various species of particle waves are emitted from the created fireball. Let us consider the particles emitted from the source according to a density distribution $\rho(r)$. The source is parametrized at the later stage of the collision where the source distribution is at the kinetic freeze-out stage. The correlation function C is defined as a ratio of the correlation intensity I_{AB} from detector A and detector B divided by the individual intensity from detector A and B, I_A and I_B , i.e., $C = I_{AB} / (I_A \cdot I_B)$.

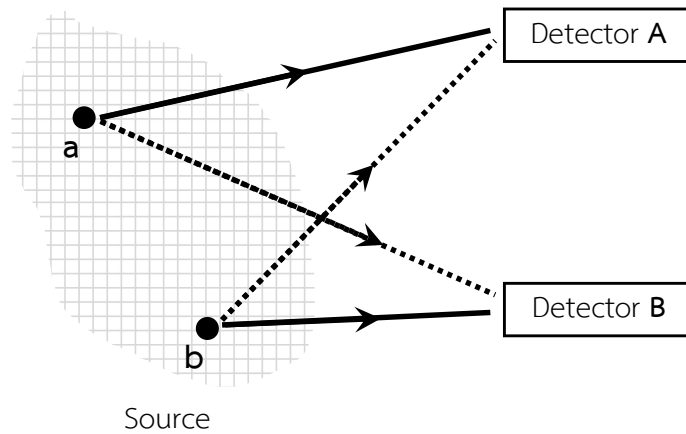


Figure 4.8 The diagram of particle detection. Particle 1 and particle 2 are emitted, with a four-momentum p_1 and p_2 , at points a and b respectively. Then they are detected by detectors A and B. If the particles are identical, we also need to consider the cases where the particles propagate indistinguishably into the detectors as illustrated with the dashed lines.

According to Figure 4.8, we can measure the correlation function by the density ratio of two-particle coincident event divided by the single particle event in phase-

space. The correlation function now reads,

$$c(\vec{k}, \vec{q}) = \frac{(d^6N/d\vec{p}_1 d\vec{p}_2)}{(dN^3/d\vec{p}_1) \cdot (dN^3/d\vec{p}_2)} = \mathcal{N} \frac{P(p_1, p_2)}{P(p_1) \cdot P(p_2)}, \quad (4.10)$$

where the relative and average momentum of the two particles are denoted by $\vec{q} = (\vec{p}_1 - \vec{p}_2)$ with $q_0 = E_1 - E_2$ and $\vec{k} = \frac{1}{2}(\vec{p}_1 + \vec{p}_2)$ with $k_0 = E_0 = \sqrt{m^2 + \vec{k}^2}$. Here, $P(p_i)$ is the probability of a single particle carrying four-momentum p_i , \mathcal{N} is a normalization factor between $P(p_1, p_2)$, the probability of the coincident event with particle 1 having four-momentum p_1 and particle 2 having four-momentum p_2 , and the product of two $P(p_i)$, the probability of an uncorrelated single particle event. We have

$$P(p_1, p_2) = \int_{\text{source}} S(x_1, p_1) S(x_2, p_2) |\phi(q, r)|^2 d^4x_1 d^4x_2, \quad (4.11)$$

where $\phi(q, r)$ is the probability amplitude for detecting two particles described with by relative four-momentum $q = p_1 - p_2$, $k = \frac{1}{2}(p_1 + p_2)$ and space-time point $r = (x_1 - x_2)$, $R = \frac{1}{2}(x_1 + x_2)$, one from point a with p_1 in detector A and one from point b with p_2 in detector B. However, since the particles of interest are identical, we cannot determine which particle is registered by A or B. So, we need to consider the exchange of two particles as a linear combination,

$$\phi(p_1, p_2) = \frac{1}{\sqrt{2}} (\phi_{12} \pm \phi_{21}) . \quad (4.12)$$

Here, ϕ_{12} (ϕ_{21}) represents the case where particle 1(2) from point a is detected in A(B) and particle 2(1) from point b in B(A). For bosons, we have a symmetric configuration (plus-sign). For fermions, we have an anti-symmetric configuration, thus a minus sign.

If a single emitted particle is described by a plane wave as a free particle, we have

$$\begin{aligned} \phi_{12} &= e^{ip_1 \cdot x_1} \cdot e^{ip_2 \cdot x_2} , \\ \phi_{21} &= e^{ip_2 \cdot x_1} \cdot e^{ip_1 \cdot x_2} , \end{aligned}$$

where the space-time coordinates of positions a and b are denoted x_1 and x_2 , respec-

tively. Now Eq. (4.11) becomes,

$$\begin{aligned}
P(\mathbf{q}, r) &= \int_{\text{source}} \mathcal{S}(\mathbf{r}) \mathcal{S}^*(\mathbf{r}) d^4 r d^4 r \\
&\quad \pm \int_{\text{source}} \mathcal{S}(\mathbf{r}) e^{i\mathbf{q}\cdot\mathbf{r}} d^4 r \mathcal{S}(\mathbf{r}) e^{-i\mathbf{q}\cdot\mathbf{r}} d^4 r \\
&= |\mathcal{F}[\mathcal{S}(0)]|^2 \pm |\mathcal{F}[\mathcal{S}(\mathbf{q})]|^2, \tag{4.13}
\end{aligned}$$

with a smoothness approximation coupled with the on-shell momentum, we can use $S(R - \frac{r}{2}, k - \frac{q}{2}) S(R + \frac{r}{2}, k + \frac{q}{2}) \simeq S(r, k) S(r, k)$, and define $\mathcal{S}(\mathbf{r}) \equiv S(\mathbf{r}) e^{i\mathbf{q}\cdot\mathbf{r}}$. For the single-particle probability, we have $P(p_i) = \int_{\text{source}} S(x_i) e^{i p_i \cdot x_i} d^4 x = \mathcal{F}[R(0)]$. Substituting into the correlation function (Eq. (4.10)), we finally end up with,

$$c(\vec{k}, \vec{q}) = 1 \pm \frac{|\mathcal{F}[\mathcal{S}(\mathbf{q})]|^2}{|\mathcal{F}[\mathcal{S}(0)]|^2}. \tag{4.14}$$

Here, we can clearly see the relation between the correlation and the source density distribution. The mass-shell constraint is $k \cdot q = 0$ and it is convenient to consider the system in the co-moving frame of the particle pair. Thus in this particle pair rest frame, the time structure of the relative source and correlation function are integrated out, i.e., $S(\vec{q}, \vec{r})$ and $C(\vec{k}, \vec{q})$. We assume a certain source function $S(\vec{q}, \vec{r})$ for the fireball and fit the result with experimental data. In this way, we can get a general idea of the size and the lifetime (Kopylov and Podgoretsky, 1972) of the emission source created by the collisions (Shuryak, 1973).

A different choice of source distribution will give us a different interpretation of the freeze-out formation. The most common parametrization for the source is the Gaussian distributions, $S(\vec{r}, t) \propto \exp(-\vec{r}^2/2R^2)$, resulting in a correlation function $C(\vec{k}, \vec{q})$ given by,

$$c(\vec{k}, \vec{q}) = 1 \pm \lambda \cdot R \exp\left(-\frac{1}{2} q^2 R^2\right). \tag{4.15}$$

The factor λ is called ‘‘chaoticity’’ or ‘‘incoherent factor’’ and added as a free parameter for a better fitting to the data (Adams et al., 2005; Adhikary et al., 2023; Weiner, 2000; Kincses et al., 2020). So far, we have discussed only the simplest example of the two-particle correlations. The correlation functions can be parametrized by various

formulae depending on the origin of correlations between considered particles.

Ref. (Chapman et al., 1995a) has shown in detail that one can assume an expanding source parametrized alternative to the Gaussian (Bertsch et al., 1988; Boal et al., 1990; Sarabura et al., 1992; Abbott et al., 1992; Seyboth et al., 1992; Chapman et al., 1995b; Roland, 1994; Heinz et al., 2002) by Yano-Koonin-Podgoretsky (Yano and Koonin, 1978) and Heinz (Chapman et al., 1995a) which is appropriate to explicitly take into account a collective cylindrical expansion, the correlation due to quantum statistics can be parametrized in terms of the components of q :

$$C(q_L, q_O, q_S) = 1 + \exp\left(-R_L^2 q_L^2 - R_O^2 q_O^2 - R_S^2 q_S^2 - 2R_{OL}^2 q_{OL}^2\right), \quad (4.16)$$

where q_i is the relative momentum of a particle pair in longitudinal q_L , outward q_O and sideward q_S directions, and R_i are the HBT radii in the same direction as defined for q_i . An advantage of using this coordinate system is that the outward radius R_O reflects the space-time structure of the source. The sideward radius R_S is separated from the temporal structure and measures a bare spatial extension. The observation of a pronounced difference of these two radii on the transverse plane, i.e., $R_O^2 - R_S^2$ or R_O/R_S , is expected to provide a hadronic signature for the realization of the new state of matter* (Chapman et al., 1995a; Ackermann et al., 2003; Heinz and Kolb, 2002; Retiere and Lisa, 2004; Kolb and Heinz, 2004; Lisa et al., 2005; Shen and Heinz, 2012). Once the quark-gluon plasma is formed, one expects that the time evolution of the system becomes slower in the phase transition (or possibly, a crossover) regime, which reflects in the long lifetime of the hadron source, and possibly a prolonged emission time.

In the above considerations, the electromagnetic interactions between charged hadrons were neglected. Namely, the quantum-statistical correlation functions discussed so far were obtained with the plane-wave assumption for the wavefunction. In the following, these will be denoted by $C_0(\vec{q}, \vec{k})$.

If the final-state electromagnetic interactions are also taken into account, the correlation function has to be calculated not via the interference of plane waves, but via the interference of solutions of the two-particle Schrödinger equation with a Coulomb-potential, describing the final state electromagnetic interactions. The ratio of these two correlation functions is called the Coulomb correction (Csorgo et al., 2004):

* Note that it has been shown in Ref. (Chapman et al., 1995a) that the interpretation for $R_O^2 - R_S^2 \propto \Delta t_{\text{emission}}$ is highly model dependent. However, only within the fixed frame, such an assumption is justified.

In order to extract the quantum-statistical effects, the counter-acting influence of the Coulomb repulsion as well as the dilution by misidentified pairs must be taken into account, while the effect of the strong interaction can be neglected (Csorgo et al., 2004; Kincses et al., 2020). This leads to the ansatz:

$$C = N \left[(1 - \lambda) + \lambda K_C(q_{inv}, R_{inv}) \cdot C_2(\vec{q}, \vec{k}) \right] \quad (4.17)$$

where λ denotes the purity of the pairs, K_C represents the Coulomb repulsion factor, and $C(q)$ is the correlation from quantum statistics parameterized by the source function. For pions, the Coulomb correction can be approximately determined from the experimental correlation function for unlike-sign pairs (Boal et al., 1990; Bowler, 1991; Baym and Braun-Munzinger, 1996), which is dominated by the Coulomb interaction and receives no contribution from Bose-Einstein correlation.

The factor $K_C(q_{inv}, R_{inv})$ describes the Coulomb interaction. It is determined as (Sinyukov et al., 1998; Csorgo, 2008; Rogochaya, 2017),

$$K = \frac{C(QS + \text{Coulomb})}{C(QS)} \quad (4.18)$$

4.5 Simulation set-ups and EoS

We use the latest version of the UrQMD transport model (UrQMD v3.5) to generate the freeze-out scenarios within heavy-ion collisions operated in various EoS modes and use the “correlation after-burner” (CRAB v3.0 β) program (Pratt, 2000) to explore the results via pion intensity interferometry.

The study will first employ three default modes within UrQMD as baseline for comparing the results from different equations of state with different types of phase transitions: I) The cascade mode is primarily used for simulating high-energy collisions where the interactions between hadrons are predominantly binary scattering and the effects of nuclear potentials become less significant compared to lower energies. Thus, in cascade mode, nuclear potentials are turned off, and interactions occur solely through binary scattering based on available cross-sections. II) The soft EoS mode is used to refer to the system with more substantial compression and less stiffening of the matter created in heavy-ion collisions. Soft EoS modes are often employed to study collisions at lower energies, where the system may spend more time in a dense, hot state before

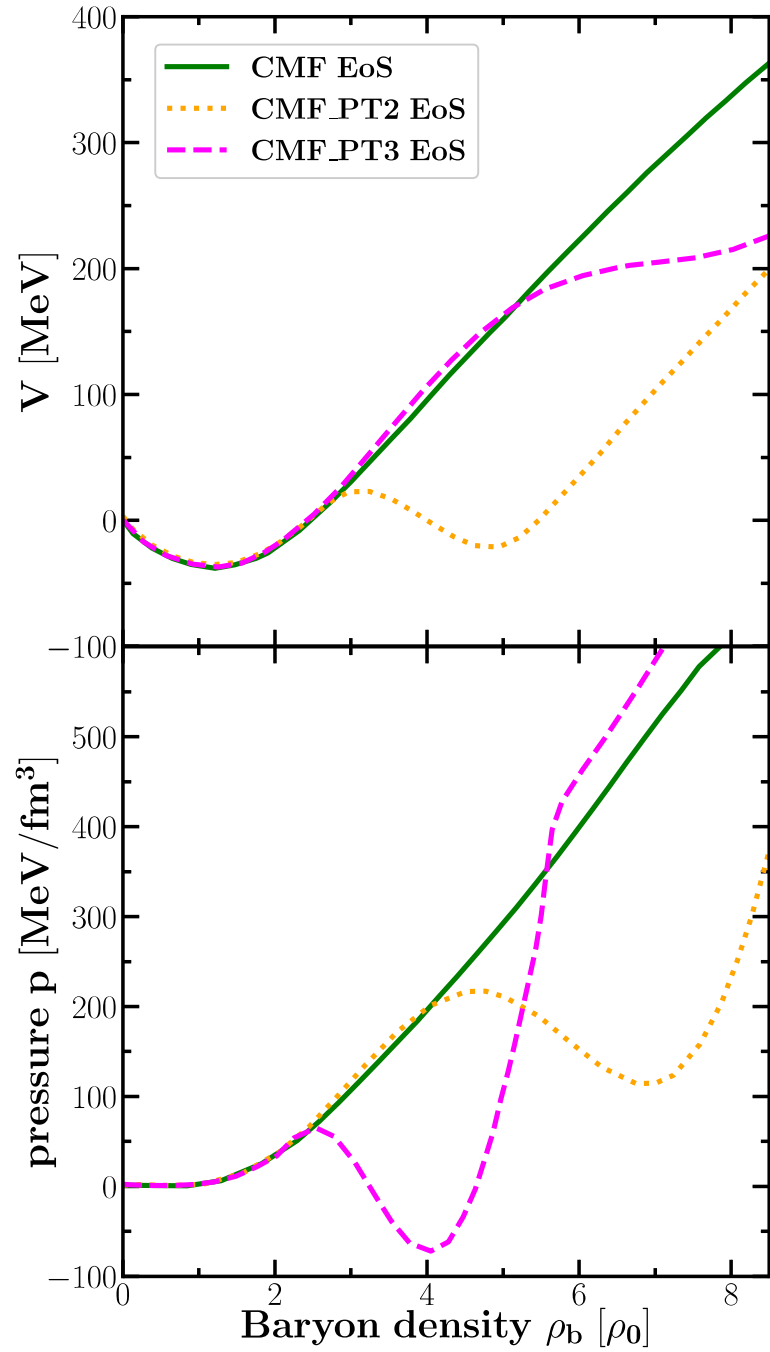


Figure 4.9 The comparison of the density dependent potential V (a) and the pressure p (b) from different the CMF EoS scenarios. CMF_PT2 EoS and CMF_PT3 EoS both are incorporated with a phase transition as well as instability region indicated by local maximum and minimum. The simple CMF EoS corresponds to a smooth crossover transition (Li et al., 2023).

expanding and cooling. The softer interactions can lead to more substantial collective flow patterns, allowing researchers to investigate the transition from the initial dense phase to the final state hadrons. At the phase transition, the system is expected to be at the softest point. III) The hard Skyrme EoS represents a scenario with less compression and more rapid expansion of the matter created in heavy-ion collisions and is often used for simulating collisions at higher energies. While this may initially suppress collective flow, the higher temperatures and densities reached in collisions at higher energies can still induce significant flow effects.

Then, we extend our investigation by adopting EoS based on chiral mean field (CMF) models (Machleidt and Entem, 2011; Omana Kuttan et al., 2022) with different phase transition scenarios to demonstrate how distinct EoS and phase transitions manifest in pion interferometry. The successful integration of CMF in the UrQMD model is done by calculating the density-dependence mean field potential energy V from the CMF model's energy per baryon as demonstrated in Figure 4.9 and also in detail in Ref. (Motornenko et al., 2020; Omana Kuttan et al., 2022).

To explore the effects of various EoS with and without different phase transition scenarios, we feed the obtained pion freeze-out phase-space coordinates at the last interactions (either collisions and decay) from UrQMD calculations to the “correlation after-burner” (CRAB v3.0 β) program (Pratt, 2000), provided by S. Pratt.

4.6 Two-Pion HBT Analysis

To begin our analysis, we want to rule out other influences or effects that could affect the final results. The Coulomb interaction could microscopically alter hadron trajectories and influences the spatial and momentum correlations at freeze-out, ultimately impacting the collective behavior of the system on the macroscopic level. Consequently, the inclusion or neglect of Coulomb interactions in HBT calculations can lead to differences in the extracted HBT radii and, thus, affect interpretations of the system size and dynamics.

Figure 4.10 compares the transverse momentum dependence (k_T) of HBT radii in central 0 — 10% Au+Au collisions at $\sqrt{s_{NN}} = 2.4$ GeV for different Coulomb interaction scenarios with the hard EoS. The analysis focuses on negative pion pairs with a pair-rapidity cut at $|y_{\pi\pi}| < 0.35$, defined as $y_{\pi\pi} = \frac{1}{2} \ln \frac{(E_1 + E_2 + p_{1,L} + p_{2,L})}{(E_1 + E_2 - p_{1,L} - p_{2,L})}$, where E_i and $p_{i,L}$ represent the energies and longitudinal momenta of each pion, respectively. This configuration aligns with the experimental data.

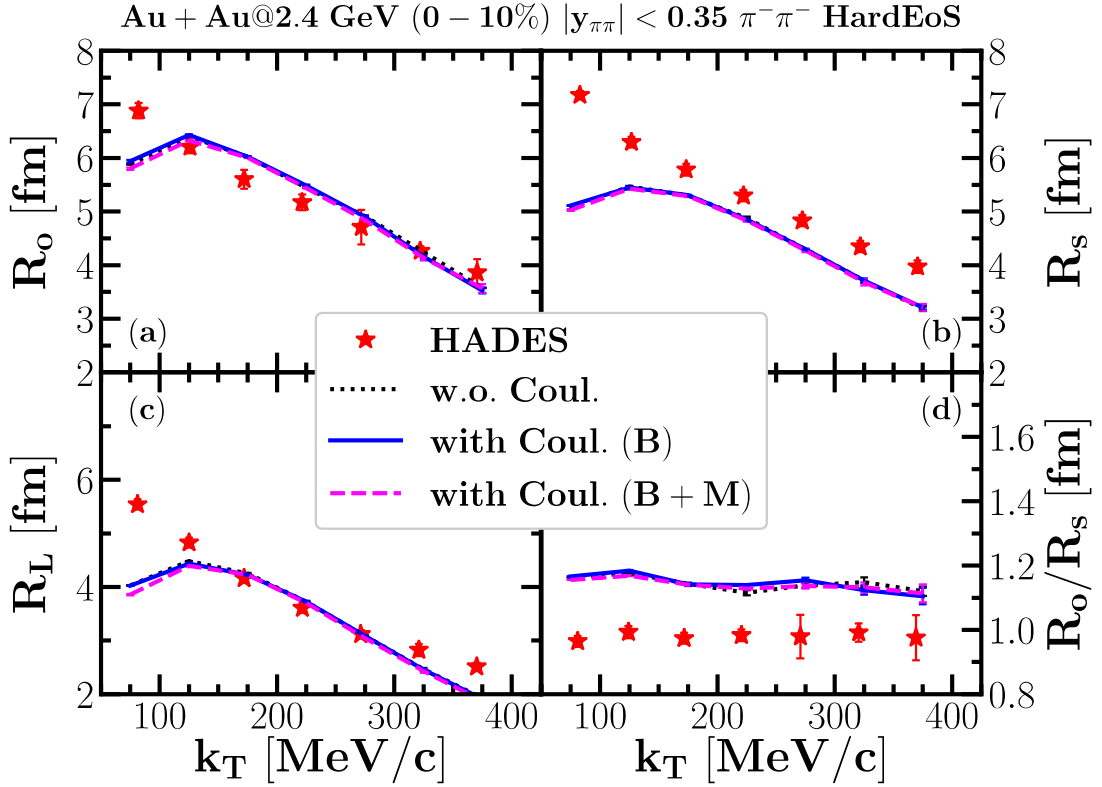


Figure 4.10 Comparison of k_T dependence of pion HBT radii showing the effect of Coulomb interactions. Panels (a), (b), and (c) display the R_0 , R_s , and R_L radii, respectively, and panel (d) shows the ratio R_0/R_s of the π -source from central (0 – 10%) Au+Au collisions at $\sqrt{s_{NN}} = 2.4$ GeV. Red star symbols depict the results from the HADES experiments (Adamczewski-Musch et al., 2019). Black dotted lines indicate the UrQMD simulation results without Coulomb potential (w.o. Coul.), blue dashed lines show the UrQMD simulation results with Coulomb potential for baryons only (with Coul. (B)), and pink solid lines depict the UrQMD simulation with the full Coulomb potential for all hadrons (with Coul. (B+M)).

At high transverse momenta ($k_T > 100$ MeV/c), all simulation scenarios can reproduce the data reasonably well, except for a slight underestimation of R_s . This underestimation leads to a higher R_0/R_s ratio compared to the measured values. Furthermore, it is clear that the impact of the Coulomb potential from both scenarios (blue dashed lines and pink solid lines) is negligible when compared to the Coulomb-free interaction (black dotted line).

Therefore, the subsequent discussion will omit the Coulomb effect on the

HBT radii. The following results will more or less come from purely nuclear potential, i.e., the choice of EoS and the phase transition.

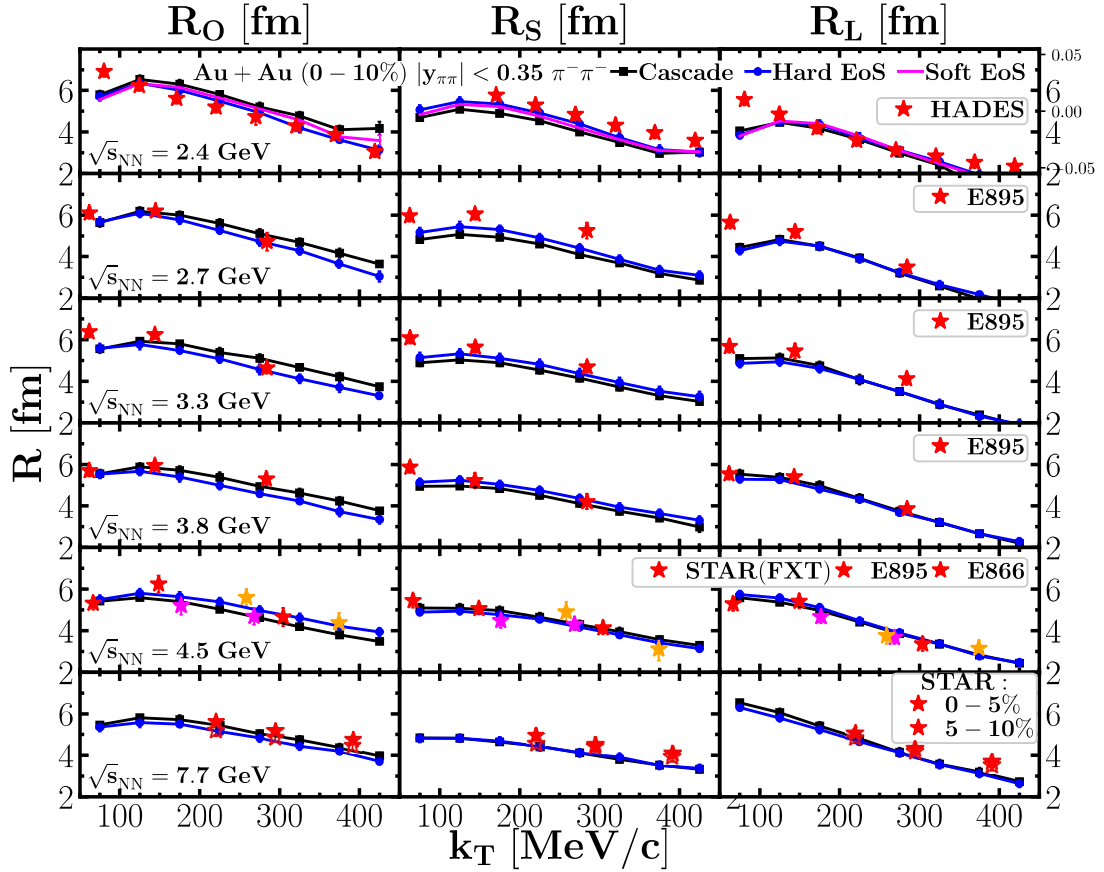


Figure 4.11 The transverse momentum (k_T) dependence of the HBT radii, R_O (left panels), R_S (middle panels), and R_L (right panels), for 0 — 10% central Au+Au collisions at $\sqrt{s_{NN}}$ ranging from 2.4 GeV (top panels) to 7.7 GeV (bottom panels). Experimental data are denoted by star symbols from HADES, E895, E866, and STAR collaborations (Lisa et al., 2000; Lisa et al., 2005; Adamczyk et al., 2015; Adamczewski-Musch et al., 2019; Adamczewski-Musch et al., 2020; Adam et al., 2021). The UrQMD simulations are represented by lines: the cascade mode (black line with square), hard EoS (blue line with circle), and soft EoS (solid pink line).

The influence of the density dependence of the nuclear potential on HBT radii is explored in Figure 4.11. The UrQMD model simulations are depicted for three scenarios: cascade mode (black line with square), hard EoS (blue line with circle), and soft EoS (solid pink line) are compared with experimental data (star symbols) (Lisa et al., 2000; Lisa et al., 2005; Adamczyk et al., 2015; Adamczewski-Musch et al., 2019; Adamczewski-

Musch et al., 2020; Adam et al., 2021) as a function of transverse momentum (k_T) within the same collision system and rapidity configuration mentioned above.

A clear impact of the nuclear potential is evident when comparing the colored lines (with nuclear potential) to the black line with squares (without nuclear potential) across the entire k_T range. This effect is particularly pronounced at lower center-of-mass energies. The hard EoS (blue line with circle) generally leads to a decrease in R_0 values and an increase in R_S compared to the cascade mode (black line with squares). This behavior results in a better description of the experimental data (star symbols) observed for most collision energies. The soft EoS (solid pink line) exhibits qualitatively similar trends to the hard EoS, hence we present the results only for $\sqrt{s_{NN}} = 2.4$ GeV for the sake of brevity.

An interesting observation is seen at $\sqrt{s_{NN}} = 4.5$ GeV, where the hard EoS predicts a higher R_0 than the cascade mode, unlike at other energies. This finding suggests a potential non-monotonic behavior in the difference between R_0 and R_S , which may not necessarily be indicative of a critical point associated with a phase transition. To gain a deeper understanding of these observations, the next section will focus on a detailed analysis of the R_0 and R_S difference across various nuclear potential scenarios, including those incorporating and excluding a phase transition.

4.7 Effect of the EoS with Phase Transition

As discussed earlier, the expected non-monotonic behavior in the R_0 and R_S difference remains ambiguous (Pratt, 2009). It's unclear whether this arises from critical behavior near the phase transition or solely from the effects of a strong repulsive potential (hard EoS). This ambiguity is further amplified by the large error bars associated with the experimental data at the relevant energy ($\sqrt{s_{NN}} = 4.5$ GeV) where the actual trend might even be a smooth increase rather than a peak (Lacey, 2015; Adamczyk et al., 2015; Adamczewski-Musch et al., 2019).

Therefore, to gain deeper insights, we explore the difference between R_0 and R_S , quantified by R_0/R_S and $R_0^2 - R_S^2$, as a function of center-of-mass energy ($\sqrt{s_{NN}}$) for various nuclear potential scenarios. These results are then compared with available experimental data, as illustrated in Figure 4.12. The R_0 and R_S values are chosen at $k_T = 275 \pm 25$ MeV/c in central (0 — 10%) Au+Au collisions with a pair-rapidity cut of $|y_{\pi\pi}| < 0.35$.

Based on our previous observations, nuclear potentials without a phase tran-

sition tend to decrease R_O and increase R_S . This explains the behavior of the hard EoS (blue line with circle) and the nuclear density dependent CMF EoS (green line), where both result in suppression of R_O/R_S and $R_O^2 - R_S^2$ compared to the cascade mode (black squares). At these energies, the hard EoS and CMF EoS potentials exhibit similar strength as the nuclear density reaches around $\rho_b/\rho_0 \leq 5$. This similarity in terms of repulsive strength results in the earlier pion emission, as aligned with the relation $\Delta\tau^2 \propto 1/(R_O^2 - R_S^2)$. Consequently, the non-monotonic behavior observed around $\sqrt{s_{NN}} \approx 4.5$ GeV in Figure 4.11 is not attributable solely to a rise in R_O from the hard EoS.

We can now shift our focus to the effects of a phase transition in the results from the CMF EoS with critical behavior representing the phase transition at $\rho_b/\rho_0 \approx 4$ and $\rho_b/\rho_0 \approx 5$ (CMF_PT2 EoS with orange dotted line and CMF_PT3 EoS with pink dashed line). At the lowest energy ($\sqrt{s_{NN}} = 2.4$ GeV), the results from all CMF EoS scenarios are similar to the ones from the hard EoS. However, as the energy increases, CMF_PT2 EoS (orange dotted line) gradually approaches the cascade scenario, reaching a maximum around $\sqrt{s_{NN}} \approx 4$ GeV. This reflects the softening of the nuclear potential due to the critical behavior from the phase transition. In contrast, CMF_PT3 EoS (pink dashed line) remains consistent with the default CMF EoS (green line) across all energies. This suggests that the nuclear density in this energy range never reaches the critical regime implied by CMF_PT3 EoS, i.e., $\rho_b/\rho_0 \approx 4 - 5$.

In conclusion, our findings indicate that HBT radii are sensitive to the EoS. CMF_PT2 suggests that critical behavior is expected around a nuclear density of $\rho_b \approx 4 - 5\rho_0$, as it best describes the experimental data at $\sqrt{s_{NN}} \approx 4$ GeV.

4.8 Space-time Structure from HBT radii

Now we continue with the discussion of the negative pion π^- emission time. The critical behavior at the phase transition may result in a softening of the EoS, leading to longer emission times. This can be interpreted in terms of the HBT radii, where $R_O^2 - R_S^2 \propto \Delta\tau_{\text{emission}}^2$ (for non-flow volume). To assess how different assumptions about the EoS affect the freeze-out time distribution, we present this comparison for various collision energies ranging from $\sqrt{s_{NN}} = 2.4 - 7.7$ GeV in Figure 4.13.

At $\sqrt{s_{NN}} = 2.4$ GeV, all the freeze-out time distributions with different EoS (colored lines) are nearly identical, except for the cascade mode (solid black line), where most pions freeze out around $t \approx 15$ fm/c. This uniformity occurs because, at

this energy, the density-dependent nuclear potentials are nearly the same.

As we move towards higher energies, the freeze-out distribution for the CMF_PT2 EoS (solid orange line) approaches that of the cascade mode, while the distributions for the other EoS remain almost identical for the rest of the energy range, with slight deviations at $\sqrt{s_{NN}} = 7.7$ GeV. Here, the freeze-out times for CMF EoS (green dashed line) and CMF_PT3 are extended similarly, while the hard EoS (solid blue line) exhibits the shortest emission times.

The corresponding mean freeze-out times $\langle t \rangle$ and transverse radii $r_T = (r_x^2 + r_y^2)^{1/2}$ of π^- are then illustrated in Figure 4.14 as functions of collision energy $\sqrt{s_{NN}}$. In panel (a), the mean freeze-out time $\langle t \rangle$ exhibits a minimum at $\sqrt{s_{NN}} \approx 4$ GeV for all calculations. The similar behaviors of increasing freeze-out time $\langle t \rangle$ at higher energies of all EoS scenarios may be attributed to resonance decay, with string excitation overcoming fragmentation. The emission time from a hard EoS (coloured line) is prolonged over the entire energy range.

Furthermore, we observe a consistent increase in transverse radii r_T in panel (b), in line with the assumption of an expanding charged volume. The transverse radii r_T from the EoS scenarios with strong repulsive potentials (colored lines) result in consistently larger r_T compared to the cascade mode (solid black line), suggesting a stronger system expansion due to higher pressure. We observe an interesting behavior of the transverse radii from the CMF_PT2 EoS (orange dotted line), where it remains relatively constant and approaches the cascade mode (solid black line).

In summary, we investigate the sensitivity of HBT radii to different Equations of State (EoS) using UrQMD simulations of central (0 — 10%) Au+Au collisions at collision energies ranging from $\sqrt{s_{NN}} = 2.4 — 7.7$ GeV. We explicitly demonstrated that the inclusion of nuclear potential, independent of Coulomb interactions, significantly impacts HBT radii (contrast to (Li et al., 2006)). We found that incorporating a hard EoS, either with or without a phase transition, leads to a better description of the experimental data for the R_O and R_S differences of the HBT radii (R_O/R_S and $R_O^2 - R_S^2$). The results obtained with the CMF_PT2 EoS exhibit a softening of the nuclear potential around $\sqrt{s_{NN}} \approx 4$ GeV due to the critical behavior, providing an even better agreement with the data compared to other EoS scenarios. This suggests that the nuclear density in this energy range falls within the region of $\rho_B \lesssim 4 — 5\rho_0$ and likely doesn't exceed these values, as the CMF_PT3 EoS doesn't exhibit any critical behavior.

Finally, we investigated the emission time, represented by the freeze-out

time distribution of negative pions π^- . Interestingly, all EoS scenarios, including the cascade mode (without any EoS), display a minimum emission time at $\sqrt{s_{\text{NN}}} \approx 4$ GeV. As expected, the freeze-out time distribution from the CMF_PT2 EoS shows a distinct behavior, with a prolonged freeze-out time approaching the cascade mode. This finding, coupled with the observation of nearly constant transverse radii until $\sqrt{s_{\text{NN}}} \approx 4$ GeV, strongly suggests a critical behavior involving a longer relaxation time associated with the softening of the nuclear EoS during the phase transition.

These results demonstrate the potential of using HBT radii as a direct probe to investigate the EoS in this density and energy regime of interest. Future studies can benefit from additional experimental data with smaller error bars to further validate and refine our understanding of the EoS in this domain.

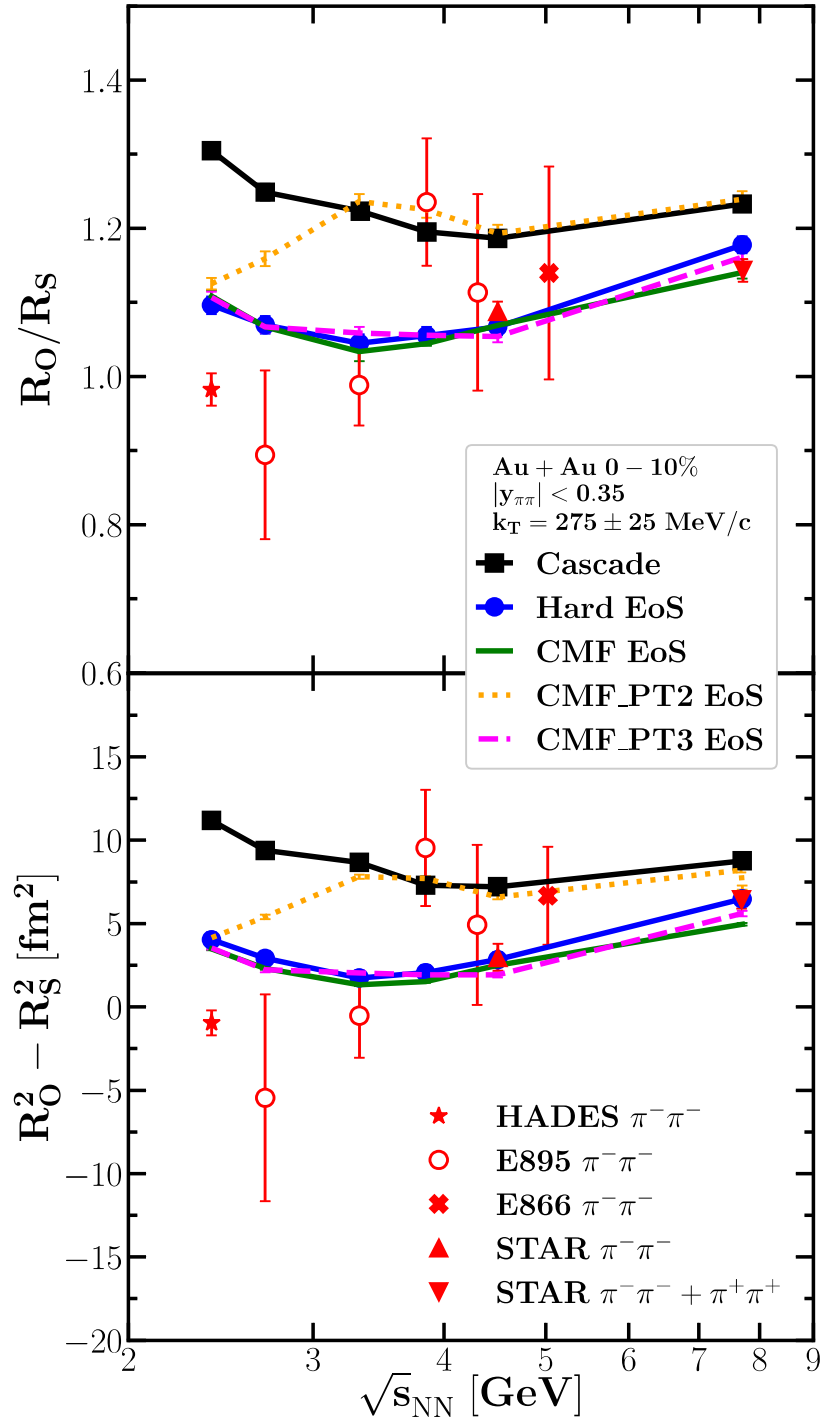


Figure 4.12 Comparison of the collision energy dependence of the (top panel) R_0/R_5 ratio and (bottom panel) $R_0^2 - R_5^2$ for cascade (black line with squares) and various EoS models (hard EoS: blue line with circles, CMF EoS: green line, CMF_PT2 EoS: orange dotted line, CMF_PT3 EoS: pink dashed line) with available experimental data (Lisa et al., 2000; Lisa et al., 2005; Adamczyk et al., 2015; Adamczewski-Musch et al., 2019; Adamczewski-Musch et al., 2020; Adam et al., 2021).

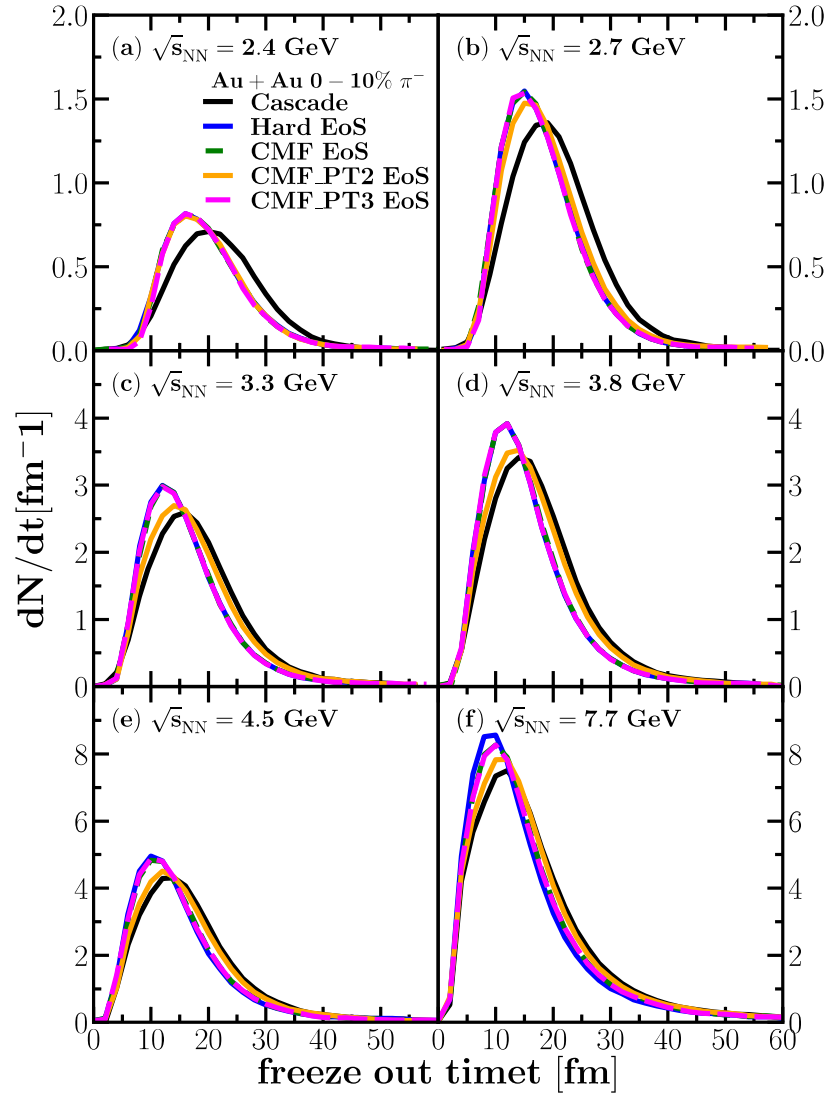


Figure 4.13 The freeze-out time distribution of π^- from 0 — 10% Au+Au collisions with the different EoS; Cascade mode (solid black line), Hard EoS (solid blue line), CMF EoS (green dashed line), CMF_PT2 EoS (solid orange line), and CMF_PT3 EoS (pink dash-dotted line)

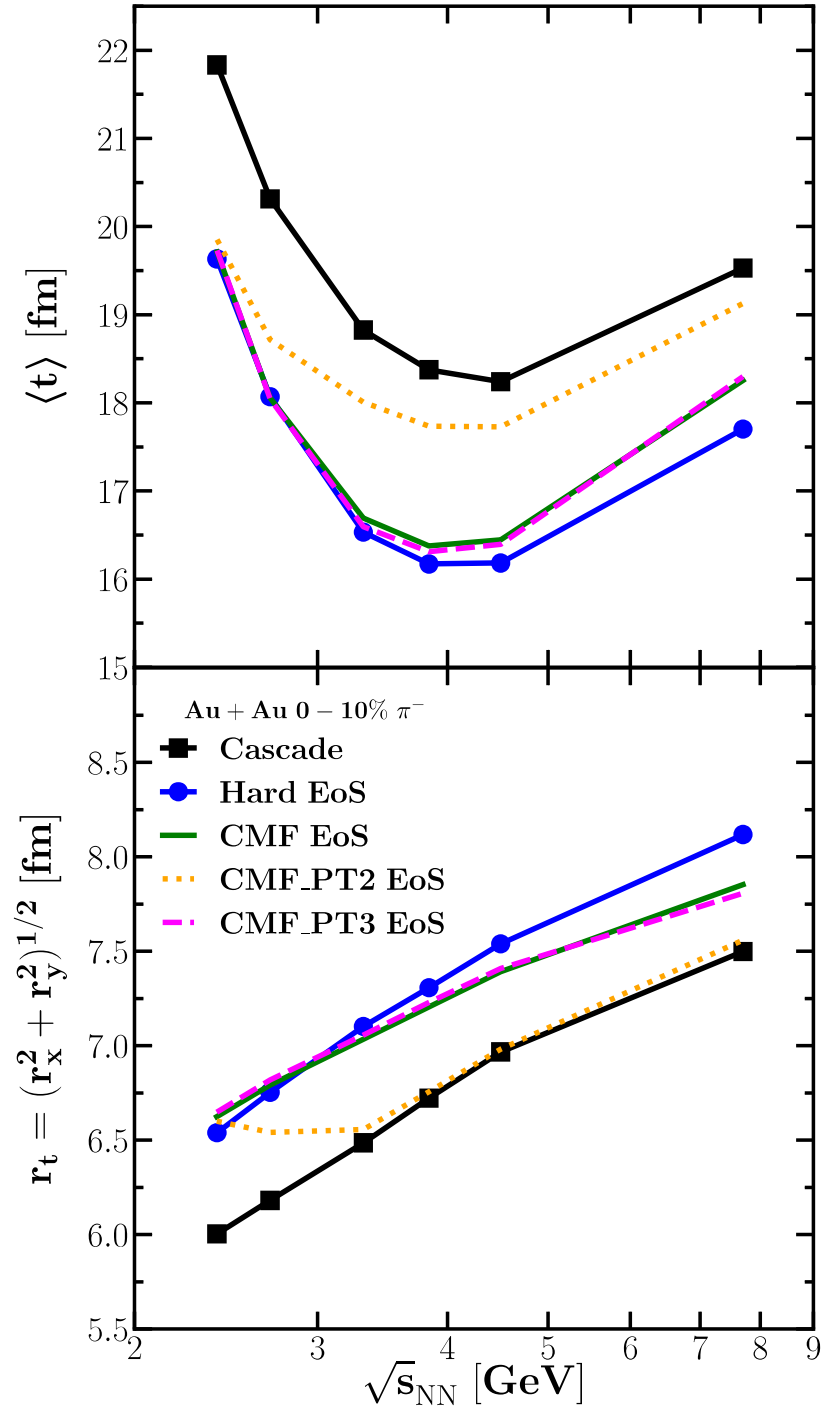


Figure 4.14 (a) The corresponding mean π^- emission time $\langle t \rangle$ and (b) transverse radii r_t at freeze-out as a function of collision energies calculated from different EoS.